

Efficient perovskite solar cells via improved carrier management

<https://doi.org/10.1038/s41586-021-03285-w>

Received: 10 June 2020

Accepted: 7 December 2020

Published online: 24 February 2021

 Check for updates

Jason J. Yoo^{1,8,9}, Gabkyung Seo^{2,7,9}, Matthew R. Chua³, Tae Gwan Park⁴, Yongli Lu¹, Fabian Rotermund⁴, Young-Ki Kim⁵, Chan Su Moon², Nam Joong Jeon², Juan-Pablo Correa-Baena⁶, Vladimir Bulovic³, Seong Sik Shin²✉, Moungi G. Bawendi¹✉ & Jangwon Seo²✉

Metal halide perovskite solar cells (PSCs) are an emerging photovoltaic technology with the potential to disrupt the mature silicon solar cell market. Great improvements in device performance over the past few years, thanks to the development of fabrication protocols^{1–3}, chemical compositions^{4,5} and phase stabilization methods^{6–10}, have made PSCs one of the most efficient and low-cost solution-processable photovoltaic technologies. However, the light-harvesting performance of these devices is still limited by excessive charge carrier recombination. Despite much effort, the performance of the best-performing PSCs is capped by relatively low fill factors and high open-circuit voltage deficits (the radiative open-circuit voltage limit minus the high open-circuit voltage)¹¹. Improvements in charge carrier management, which is closely tied to the fill factor and the open-circuit voltage, thus provide a path towards increasing the device performance of PSCs, and reaching their theoretical efficiency limit¹². Here we report a holistic approach to improving the performance of PSCs through enhanced charge carrier management. First, we develop an electron transport layer with an ideal film coverage, thickness and composition by tuning the chemical bath deposition of tin dioxide (SnO_2). Second, we decouple the passivation strategy between the bulk and the interface, leading to improved properties, while minimizing the bandgap penalty. In forward bias, our devices exhibit an electroluminescence external quantum efficiency of up to 17.2 per cent and an electroluminescence energy conversion efficiency of up to 21.6 per cent. As solar cells, they achieve a certified power conversion efficiency of 25.2 per cent, corresponding to 80.5 per cent of the thermodynamic limit of its bandgap.

SnO_2 -based electron transport layers (ETLs) offer favourable band alignment, while being processable at low temperature^{13–18}. Of the various deposition methods, SnO_2 nanoparticle-based ETLs have demonstrated the best performances thus far. However, SnO_2 nanoparticle-based PSCs exhibit relatively low electroluminescence external quantum efficiency (EQE) values, and hence higher open-circuit voltage (V_{OC}) deficits (defined as the radiative V_{OC} limit minus the high V_{OC}), compared to TiO_2 -based PSCs⁸, in spite of efforts to eliminate non-radiative recombination pathways¹⁹. The electroluminescence EQE of a photovoltaic device, determined by measuring the luminescence efficiency under forward bias, is a direct measure of the radiative efficiency of carrier recombination. The electroluminescence EQE can be used to quantify the non-radiative contribution to the V_{OC} deficit via the reciprocity theorem, and is a useful metric for solar cell characterization^{11,20}. Thus, it is crucial to develop strategies that minimize photovoltage losses at

the ETL/perovskite interface so as to minimize the V_{OC} deficit, encouraging the search for a different deposition method that can develop the full potential of SnO_2 ETLs. The ideal SnO_2 ETL will generate a high photovoltage and fill factor by having complete and conformal coverage without pinholes, an ideal band alignment to efficiently extract electrons while blocking hole back-transfer, a low defect density to prevent detrimental interface recombinations, and will also be thin enough to promote efficient charge extraction²¹.

As a part of our holistic approach, we first report a facile method of chemically tuning the physical and electronic properties of the SnO_2 ETL via chemical bath deposition. Chemical bath deposition enables uniform and complete coverage of the underlying substrate by depositing a dense and conformal layer^{22,23}. However, a lack of understanding of the complex chemical reactions during SnO_2 chemical bath deposition has prevented the fabrication of highly efficient PSCs. We infer that the

¹Department of Chemistry, Massachusetts Institute of Technology, Cambridge, MA, USA. ²Division of Advanced Materials, Korea Research Institute of Chemical Technology, Daejeon, Republic of Korea. ³Department of Electrical Engineering and Computer Science, Massachusetts Institute of Technology, Cambridge, MA, USA. ⁴Department of Physics, Korea Advanced Institute of Science and Technology, Daejeon, Republic of Korea. ⁵Central Research Facilities, Ulsan National Institute of Science and Technology (UNIST), Ulsan, Republic of Korea. ⁶School of Materials Science and Engineering, Georgia Institute of Technology, Atlanta, GA, USA. ⁷Department of Energy Science, Sungkyunkwan University, Suwon, Republic of Korea. ⁸Present address: Division of Advanced Materials, Korea Research Institute of Chemical Technology, Daejeon, Republic of Korea. ⁹These authors contributed equally: Jason J. Yoo, Gabkyung Seo. ✉e-mail: sss85@kRICT.re.kr; mgb@mit.edu; jwseo@kRICT.re.kr

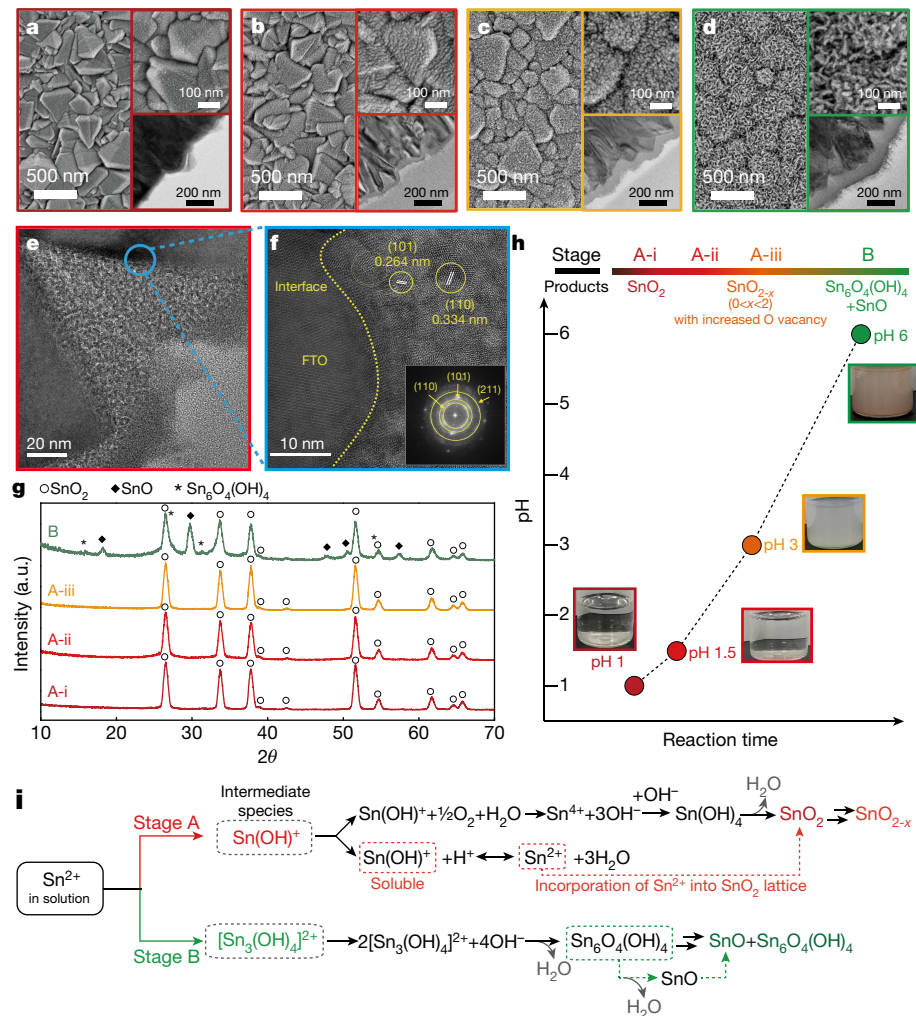


Fig. 1 | Synthesis and characterization of tin oxide film on FTO. **a–d**, Top-view SEM images synthesized for increasing time, leading to an increased pH: **a**, stage A-i; **b**, stage A-ii; **c**, stage A-iii; and **d**, stage B. The top-right insets show a zoomed-in SEM and the bottom-right insets show the corresponding cross-sectional TEMs. **e, f**, High-resolution TEM images of films prepared up to

stage A-ii (the inset in **f** shows a fast Fourier transform pattern of the TEM image). **g**, X-ray diffraction patterns of the SnO₂ layer at different reaction stages. a.u., arbitrary units. **h**, Schematic illustration of the reaction progress with photograph of the reaction solution at each stage. **i**, Schematic illustration of the overall reaction mechanism for the formation of the SnO₂-based films.

Sn intermediate species during chemical bath deposition play a crucial part in the quality and the characteristics of the final SnO₂ layer. More specifically, we suggest that the formation of various Sn intermediate species depends on the decomposition pathway of the Sn²⁺ precursor (SnCl₂), which depends on the pH of the reaction solution^{24–26}.

Synthesis and characterization of SnO₂

Freshly prepared chemical bath deposition solutions exhibit pH < 1 and the pH increases with longer reaction time as urea decomposes and releases OH[−] (Supplementary Fig. 1). We divide the changes in the thin film properties of the SnO₂ layer with reaction time into two main stages as shown in Fig. 1. Stage A shows the growth of SnO₂ layer with planar morphologies. Within stage A, stage A-i at early reaction times is the most acidic (pH 1), followed by stage A-ii (pH 1.5) and stage A-iii (pH 3). Stage B is the final stage of the reaction with a distinct morphology of interconnected nanorods and has the highest pH of 6.

Figure 1a–d shows scanning electron microscope (SEM) images of the SnO₂ layer deposited on top of a fluorine-doped tin oxide (FTO)-covered glass via chemical bath deposition. The top-right insets are magnified top-down SEM images, highlighting the roughness and surface morphology of the film, with the SnO₂ layer more clearly seen on top

of a pyramid-shaped FTO domain. The insets on the bottom-right are cross-section transmission electron microscope (TEM) images. In the early stage of the reaction (stage A-i), which is when the pH of the reaction solution is still approximately 1, the SnO₂ layer is about 20 nm thick, conformal with the underlying FTO layer. With increasing reaction time, and thus an increase in the pH of the reaction solution, the size of the SnO₂ domain increases while forming a densely packed layer with thicknesses ranging from around 50 nm to around 100 nm (Fig. 1b, c). When the reaction reaches stage B, the SnO₂ begins to grow into elongated rod-like morphologies (Fig. 1d).

The high-resolution TEM shown in Fig. 1b (stage A-ii) shows a SnO₂ layer forming complete coverage with interconnected domains, even down to the sharp valleys within the FTO layer (Fig. 1e). The conformal and complete SnO₂ coverage is further confirmed by cyclic voltammetry, which shows that the films have robust hole-blocking capabilities when reacted past stage A-ii, or pH 1.5 (Supplementary Fig. 2), whereas stage A-i SnO₂ is inefficient at hole blocking. The lattice fringes in Fig. 1f indicate that individual domains have high crystallinity, where the lattice fringes correspond to the (110) and (101) planes of rutile SnO₂, with the fast Fourier transform pattern of the TEM image shown in the inset to Fig. 1f. The films prepared while still under acidic conditions (stages A-i, A-ii and A-iii) have a

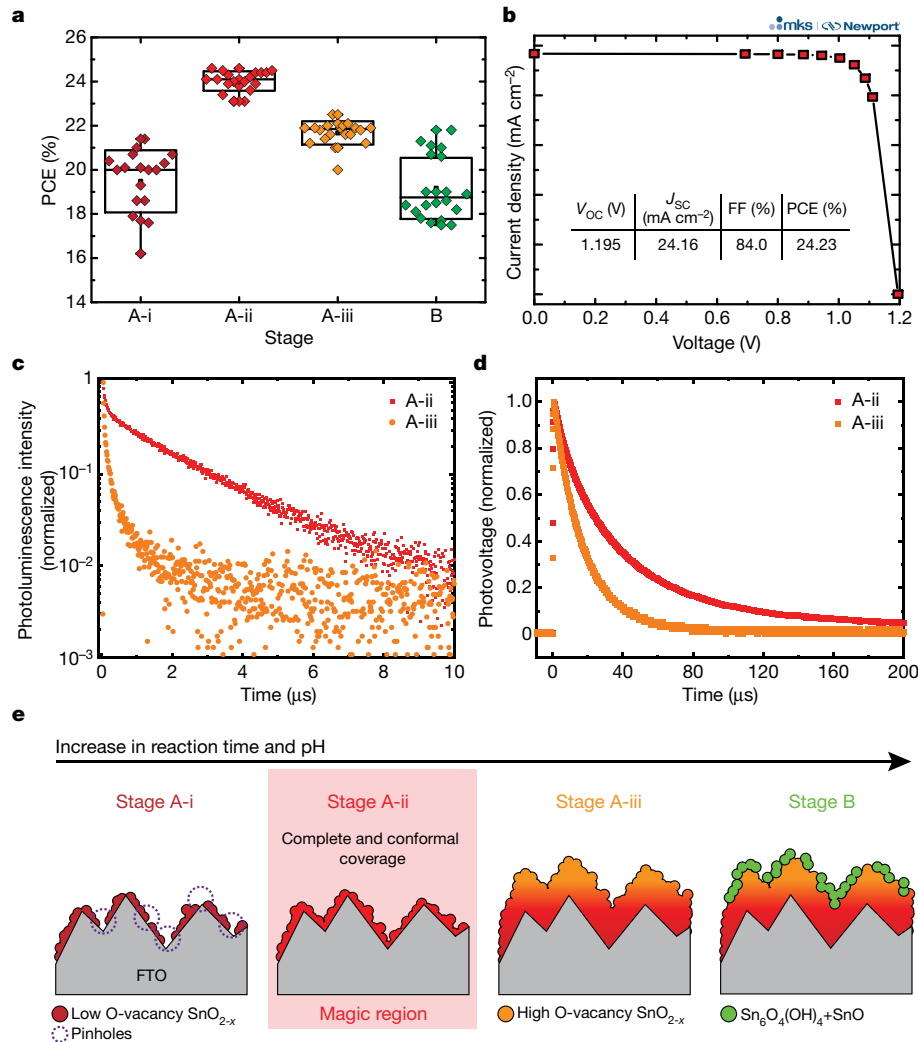


Fig. 2 | Solar cell performance of PSCs based on various SnO_2 ETLs. **a**, PCE statistics represented in box-and-whisker plots (centre line, average; box limit, standard deviation; whiskers, outliers) for PSCs based on SnO_2 ETL synthesized up to various stages: stage A-i, A-ii, A-iii and B. **b**, Quasi-steady-state current density versus voltage (J - V) curve of the best-performing device (stage A-ii) certified at Newport (MKS Instruments). The device exhibits a PCE of 24.2% from the quasi-steady-state measurement. The perovskite composition is FAPbI_3 with an added 5 mol% MAPbBr_3 , J_{SC} , the short-circuit current; FF, fill factor. **c**, Time-resolved photoluminescence traces for perovskite thin film deposited on stage A-ii SnO_2 (red trace) or stage A-iii SnO_2 (orange trace). The average lifetime for the stage A-ii sample and the A-iii sample is 984 ns and 81 ns,

respectively. The reduced carrier lifetime for the stage A-iii SnO_2 sample indicates heavy non-radiative recombination at the interface, whereas a favourable interface is achieved for the stage A-ii SnO_2 sample. **d**, Transient photovoltage traces for stage A-ii SnO_2 - and stage A-iii SnO_2 -based perovskite solar cells. The decay time, determined as the time it takes to each 1/e intensity, for stages A-ii and A-iii is 37.8 μs and 17.9 μs , respectively. The longer decay time for the A-ii SnO_2 -based device further suggests reduced non-radiative recombination at the interface. **e**, Schematic illustration of the progress of the reaction highlighting stage A-ii as the ‘magic region’, which exhibits ideal film coverage, morphology and chemical composition.

pure phase, whereas films prepared by allowing the reaction solution to reach stage B contain secondary phases, such as $\text{Sn}_6\text{O}_4(\text{OH})_4$ and SnO (Fig. 1g).

SnO_2 synthesis mechanism

From the experimental results, we classify the reaction progress into four parts (Fig. 1h). At the beginning of the reaction (stages A-i and A-ii, pH = 1–1.5), the dominant product of the chemical bath deposition reaction is SnO_2 . As the reaction progresses to stage A-iii, owing to a sharp decrease in oxygen dissolved in the reaction solution, incomplete oxidation of Sn^{2+} to Sn^{4+} is highly likely (Supplementary Fig. 3). This leads to dominant production of SnO_{2-x} (ref. ²⁴). In addition, the chemical bath deposition solution turns murky around this reaction stage, owing to the formation of insoluble amorphous tin oxide species (inset in Fig. 1h)²⁴. When the reaction reaches stage B, oxygen-deficient

SnO_{2-x} is joined by $\text{Sn}_6\text{O}_4(\text{OH})_4$ and SnO , which are produced as secondary phases (red precipitate shown in the inset), as observed from the X-ray diffraction data (Fig. 1g and Supplementary Fig. 4).

We propose a synthesis mechanism during the chemical bath deposition growth of SnO_2 in Fig. 1i. In stage A, the Sn^{2+} ions dissolved in strong acidic aqueous solution undergo a hydrolysis reaction, and form $\text{Sn}(\text{OH})^+$ intermediate species. $\text{Sn}(\text{OH})^+$ is then oxidized to Sn^{4+} by the dissolved oxygen in the solution²⁴. The Sn^{4+} ions then react with OH^- ions, provided by the decomposition of urea, to form $\text{Sn}(\text{OH})_4$ species, which are converted to SnO_2 via a dehydration reaction (top branch in Fig. 1i)^{24,27}. However, Sn^{2+} ions from $\text{Sn}(\text{OH})^+$ can then be readily incorporated into the SnO_2 lattice owing to the comparable ionic radii of Sn^{2+} (0.62 Å) and Sn^{4+} (0.69 Å) for hexa-coordinated Sn species (middle branch in Fig. 1i)^{28–30}. The incorporation of Sn^{2+} into the SnO_2 lattice leads to the formation of oxygen vacancies in the SnO_2 layer to preserve charge neutrality. This leads to nonstoichiometric SnO_{2-x} ,

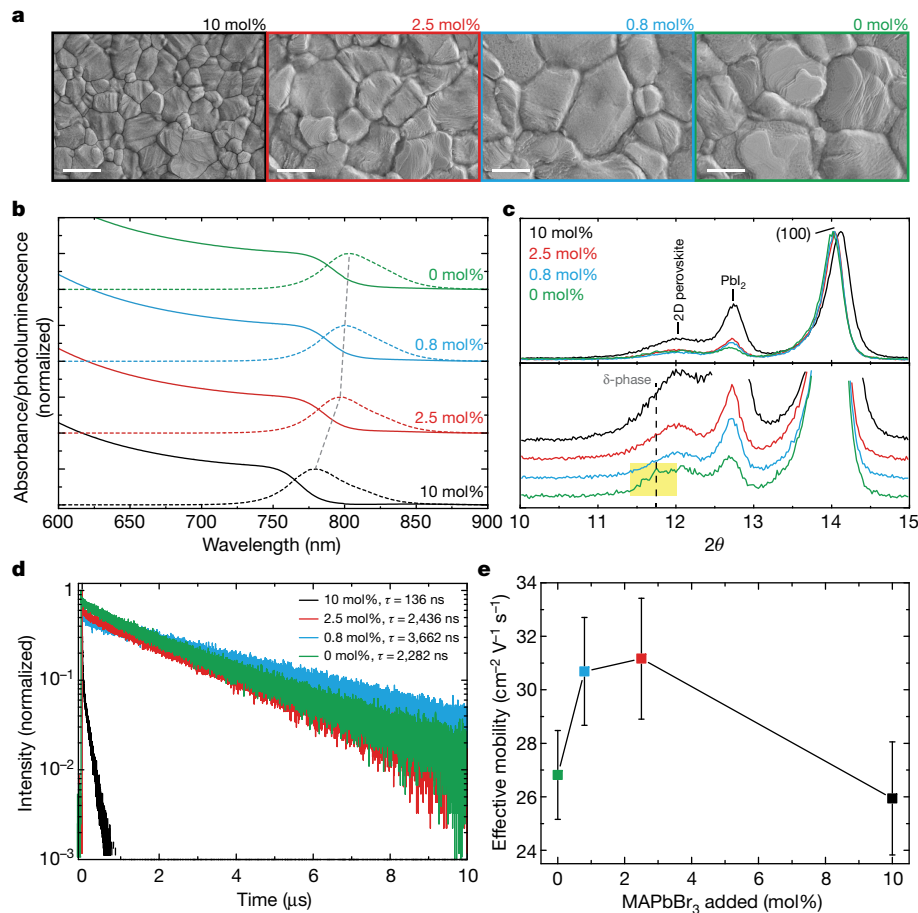


Fig. 3 | Characterization of perovskite thin films varying the mole per cent of MAPbBr₃ added. **a**, SEM images of perovskite thin films with decreasing amounts of added MAPbBr₃ (from 10% to 0%). The scale bars are 1 μm. **b**, Ultraviolet-visible absorbance and photoluminescence spectra of perovskite thin films with various amounts of MAPbBr₃ added. **c**, X-ray diffraction of perovskite thin films with four different amounts of MAPbBr₃ added. The diffraction peaks for two-dimensional perovskite, Pbl₂, and the (100) phase are shown. The bottom panel is the zoomed-in view of the top,

where the position of the δ-phase is displayed as the dotted line and the diffraction peaks that corresponds to the δ-phase is highlighted in yellow. The perovskite thin film without any MAPbBr₃ (0 mol%) shows detectable amount of δ-phase. **d**, Time-resolved photoluminescence traces for perovskite thin films with decreasing amounts of added MAPbBr₃. Carrier lifetimes τ are obtained from a mono-exponential fit. **e**, Effective mobility for perovskite thin films determined from optical pump–terahertz probe measurements (error bars show one standard deviation).

which is synthesized in stage A-iii, as a result of a sharp decrease in oxygen dissolved in the reaction solution. When the reaction reaches stage B, a different Sn intermediate species, Sn₃(OH)₄²⁺, forms in the reaction^{25,31}. The Sn₃(OH)₄²⁺ intermediate species can undergo a condensation reaction when the pH is sufficiently high, resulting in Sn₆O₄(OH)₄ (refs. ^{25,26,32}). The Sn₆O₄(OH)₄ is then partially transformed to SnO via a dehydration reaction, producing a mixture of Sn₆O₄(OH)₄ and SnO (bottom branch in Fig. 1*i*), consistent with the X-ray diffraction results^{26,33}.

SnO₂ ETL-based PSCs

We fabricated a series of PSCs up to different stages for the growth of the SnO₂ layer to evaluate device performance (Fig. 2). PSCs with stage A-i SnO₂ show an average efficiency of about 20% with a relatively wide power conversion efficiency (PCE) distribution (Fig. 2a). A noticeable improvement in device performance is observed for stage A-ii SnO₂, where the PCE exceeds 24%, with the greatest improvements in V_{oc} and fill factor (Supplementary Fig. 5). These devices show a stabilized power output of up to 24.5% with a certified quasi-steady state PCE up to 24.2% (Fig. 2b and Supplementary Figs. 6–9). We attribute this substantial advancement in device performance to complete and conformal coverage of the SnO₂ layer, which prevents interfacial

recombination. In contrast, when the reaction reaches stage A-iii, we observe a noticeable drop in device performance, with the greatest contribution from lower fill factor and V_{oc} values despite complete film coverage and no detectable non-SnO₂ phases. To understand this device result, we performed time-resolved photoluminescence and transient photovoltage measurements to probe the interaction between the SnO₂ layers (stages A-ii and A-iii) and the perovskite active layer carefully (Fig. 2c, d).

Defects within a solar cell act as a carrier trap sites where the energy is lost through non-radiative recombination pathways. Thus, an ideal solar cell should be free from such trap sites. We performed time-resolved photoluminescence measurements because detrimental interfacial trap states lead to reduced carrier lifetimes. The time-resolved photoluminescence results show a much shorter carrier lifetime for stage A-iii SnO₂ than for stage A-ii samples, indicating an increase in non-radiative interfacial recombination between SnO₂ and perovskite, and thus leading to lower photovoltage and fill factor. From transient photovoltage measurements, we confirmed much longer decay times in stage A-ii devices than in stage A-iii PSCs, which further indicates reduced non-radiative pathways for stage A-ii SnO₂-based devices.

Inferior device performance for stage A-iii SnO₂ devices is the result of reduced carrier lifetime, where the increase in defects in the SnO₂ layer is responsible for an increase in non-radiative recombination

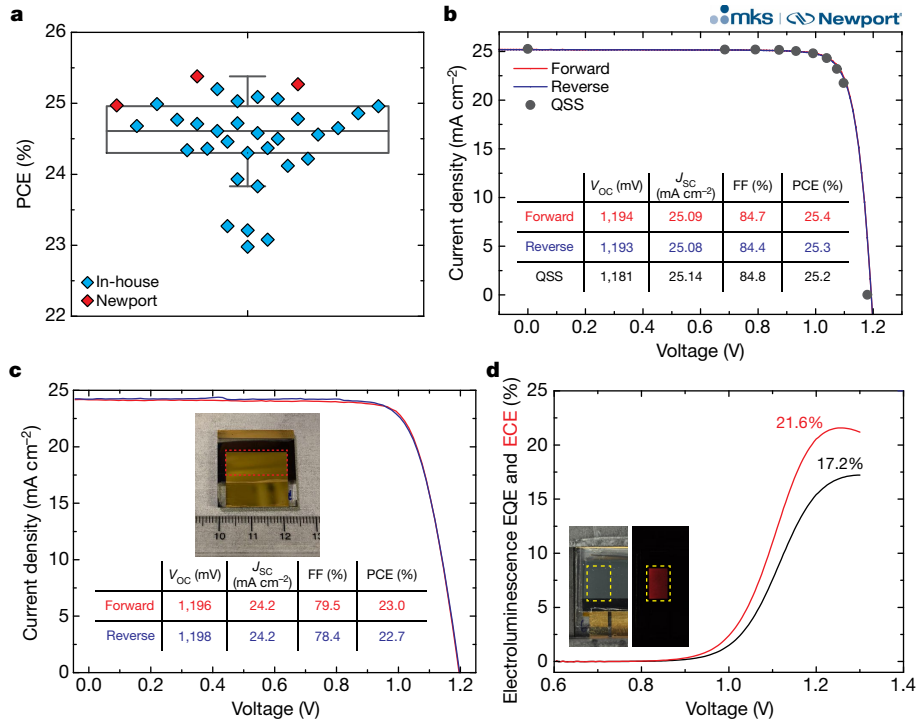


Fig. 4 | Device result for best-performing PSCs with 0.8 mol% MAPbBr₃. **a**, Statistical distribution represented in box-and-whisker plots (centre line: average, box limit: standard deviation, whiskers: outliers) for best-performing PSCs (0.0937 cm² active area defined by a mask aperture). Devices with high and stable PCEs were then encapsulated and antireflective films were applied before testing at Newport. The blue points show the PCE values measured in-house and the red points show the PCE values measured at Newport for certification purposes. **b**, J - V curves of the champion device measured at

Newport, showing both the conventional J - V sweep and the certified quasi-steady-state measurements. **c**, J - V curves of a larger-area PSC exhibiting a PCE up to 23%. The active area is 0.984 cm², defined by a mask aperture. The inset is a photograph, where the dotted outlines approximate the mask aperture. **d**, Electroluminescence EQE and ECE values of our PSC under forward bias. Their maximum values are given. The inset shows the device (left photograph) with visible red emission upon voltage bias (right photograph).

pathways. In metal oxide thin films, oxygen vacancies act as site defects; their negative effects are especially important in films composed of tiny domains with high surface areas, such as in our SnO₂ films synthesized via chemical bath deposition.

Both X-ray photoelectron spectroscopy and ultraviolet-visible absorption spectroscopy suggest higher concentrations of defects for stage A-iii SnO₂, as a form of oxygen vacancy, shown by the shift of the Sn 3d_{5/2} state towards lower binding energy (Supplementary Fig. 10a)^{28,30,34–36}, gradual increase in absorptivity in the ultraviolet-blue wavelength range (Supplementary Fig. 10b), and higher Raman signal (Supplementary Fig. 11). The uncontrolled formation of defects in stage A-iii SnO₂ films not only increases charge recombination at the SnO₂/perovskite interface, but also limits electron transport through SnO₂ nanodomains (Supplementary Fig. 12). On the other hand, the suppressed formation of surface defects for stage A-ii SnO₂ films is critical for realizing high fill factor and a low V_{OC} deficit, along with appropriate surface coverage (Supplementary Fig. 13).

In addition, the ETL needs to have a deep relative valence band in order to efficiently prevent hole quenching at the ETL/perovskite interface. Ultraviolet photoelectron spectroscopy shows that the deepest valence band is achieved during stage A-ii (Supplementary Fig. 14). This further supports the reduction of charge recombination in the device and thus the high efficiency observed for PSCs fabricated using stage A-ii SnO₂ (ref. ³⁷). Lastly, the PSCs with stage B SnO₂ show the lowest PCE, probably owing to the formation of non-SnO_{2-x} phases, such as Sn₆O₄(OH)₄ and SnO, which are not electron-transporting, along with overproduction of oxygen vacancies in the SnO₂ layer. The overall understanding of the chemistry during the synthesis of SnO₂ via chemical bath deposition is illustrated in Fig. 2e (see Methods for a detailed discussion).

Effect of the MAPbBr₃ additive

In addition to engineering the physical and electrical properties of the ETL, further improvements in PSC performance can be achieved by improving the optoelectronic properties of the perovskite active layer. An ideal active layer should present a high absorption profile to maximize carrier generation with long carrier lifetimes and mobilities for efficient carrier collection. This requires developing strategies to improve crystal grain size and carrier lifetime, while preventing the formation of detrimental traps at the bulk and interfaces. Notably, improving the efficiency of PSCs requires the decoupling of the passivation strategies for the bulk and the interface because the type and concentration of defects affect them differently. In the second part of our holistic approach, we show that only a trace amount of methylammonium lead bromide (MAPbBr₃) (<1 mol%) is needed to stabilize the perovskite active layer, with the benefit of improved optoelectronic properties.

Figure 3 shows the characterization of perovskite thin films passivated with a two-dimensional perovskite, with the bulk perovskite fabricated with the addition of various amounts of MAPbBr₃. An increase in grain size with decreasing amounts of MAPbBr₃ is clear in the SEM images of Fig. 3a. The correlation suggests that MAPbBr₃ arrests perovskite grain growth, probably owing to the slow diffusion of the large bromide anion³⁸ in a perovskite thin film fabricated with methylammonium chloride (MACl) additives, where MACl has been reported to promote perovskite crystal grain growth.

In addition to changes in grain size and morphology, the absorption onset and the photoluminescence peak redshifts are consistent with decreased incorporation of MAPbBr₃ into the perovskite crystal as lower amounts of MAPbBr₃ are added (Fig. 3b). Notably, X-ray diffraction

analysis shows successful passivation of the perovskite active layer from the detrimental formamidinium lead iodide (δ -FAPbI₃) phase with a MAPbBr₃ concentration as low as 0.8 mol% (Fig. 3c)^{39,40}. Such a low concentration is in contrast to the commonly used range of 7–20 mol%, which was established through processes that passivate both the bulk and the interface in one step. We believe stabilization of the intermediate phase, before thermal annealing, is responsible for successful stabilization of α -FAPbI₃, even at such a low MAPbBr₃ concentration (Supplementary Figs. 15, 16). The two-dimensional perovskite passivation we used is thus shown to be effective in stabilizing the interface, which is prone to the formation of defects and the unfavourable δ -phase^{8,41}.

Carrier lifetimes can be determined through fitting the time-resolved photoluminescence decays to a mono-exponential function (Fig. 3d). Films with MAPbBr₃ added below 2.5 mol% show substantially longer carrier lifetimes than the 10 mol% sample, with the longest carrier lifetime observed in the 0.8 mol% sample (>3.6 μ s). Carrier lifetimes in the microsecond range suggest that there are few non-radiative pathways and such long carrier lifetimes can lead to high V_{OC} . We attribute the long carrier lifetimes to a combination of increased perovskite crystal grain size and successful passivation using the two-dimensional perovskite. Detrimental halide segregation, which is suspected to form carrier trap sites, is likely to be reduced at low MAPbBr₃ concentrations and this may also contribute to the increased carrier lifetimes^{8,42}.

Carrier dynamics can be obtained using optical pump–terahertz probe spectroscopy, measuring transient photoconductivity ($-\Delta T/T$) at different carrier densities (Fig. 3e and Supplementary Fig. 17). With an increase in fluence, and thus an increase in carrier density, the $-\Delta T/T$ increases and the decay trace develops a fast component corresponding to increasing higher-order recombinations. An effective mobility can be calculated from the recombination dynamics measured by optical pump–terahertz probe measurements⁴³. Figure 3e plots effective mobilities as a function of the mole per cent added MAPbBr₃. Interestingly, the effective mobility increases from 0 mol% to 2.5 mol% ($26.8 \text{ cm}^2 \text{ V}^{-1} \text{ s}^{-1}$) to 31.2 $\text{cm}^2 \text{ V}^{-1} \text{ s}^{-1}$), before dropping down to 25.9 $\text{cm}^2 \text{ V}^{-1} \text{ s}^{-1}$ for 10 mol%. Indeed, as we have observed for grain sizes (Fig. 3a) and carrier lifetimes (Fig. 3d), this low-concentration region can yield large changes in morphologies and carrier dynamics, which correlate with effective mobility. It is also possible that the perovskite crystal orientation, which is known to influence effective mobilities⁴⁴, and homogenization of halides may also be affected at low concentrations of added MAPbBr₃. Thus, through separately passivating the bulk (with extremely low amounts of MAPbBr₃) and the interface (with two-dimensional perovskite passivation⁸), highly efficient PSCs can be fabricated by substantially reducing the MAPbBr₃ concentration, with the added benefit of reducing the bandgap penalty.

Solar cell and electroluminescence performance

PSCs were fabricated by combining our newly developed SnO₂ ETL and the improved perovskite layer described above. These PSCs show an average PCE of 24.7%, with some devices exceeding a PCE of 25%, when measured in-house (blue data points, Fig. 4a). The best performing devices were sent to the solar cell device testing facility in Newport, USA, for certification with the test results shown as the red data points in Fig. 4a. The best-performing device achieved a certified PCE of 25.2% from a quasi-steady-state measurement, with PCEs determined from the current–voltage (J – V) sweep to be 25.3% and 25.4% for the reverse and forward sweep, respectively (Fig. 4b and Supplementary Figs. 18–21)⁴⁵. In addition, the certified device showed almost no change in PCE during up to 3,600 h of storage (Supplementary Fig. 22). Additionally, the encapsulated device retained about 80% of its initial PCE after 500 h under continuous light illumination at maximum power point (100 mW cm⁻², AM1.5G, 45 °C), without an ultraviolet cut filter (Supplementary Fig. 23). We also fabricated PSCs with larger areas; our best-performing large-area cell (0.984 cm²) exhibits PCEs up to 23.0% with a high V_{OC} value of 1,196 mV (Fig. 4c).

The bandgap of this record cell, $E_g = 1.56 \text{ eV}$, was determined from the inflection point of the EQE curve (Supplementary Fig. 24)¹¹. This bandgap corresponds to a thermodynamic PCE upper limit of 31.3%. At 25.2% PCE, our best-performing certified cell is thus at 80.5% of the theoretical efficiency limit, which is comparable to the best Si solar cells, which are at 80.9% of the theoretical limit⁴⁶.

We attribute the high PCEs of our cells to major improvements in the V_{OC} and the fill factor. The radiative V_{OC} limit V_{OC}^{rad} is calculated to be 1.270 V and the V_{OC} measured without an aperture mask reaches 1.225 V (Supplementary Fig. 25)^{6,11,47}, resulting in a ratio of V_{OC} to the radiative V_{OC} limit of up to 96.5%, which is the highest reported thus far for a PSC, and is within striking distance of that for GaAs (97.7%). Such a low V_{OC} deficit suggests that almost all non-radiative recombination pathways have been efficiently eliminated and that these PSCs should be highly luminescent when operated as a light-emitting diode, as we find below.

Figure 4d shows a plot of the electroluminescence EQE and energy conversion efficiency (ECE) values versus voltage of a PSC measured under forward bias (the current–luminance–voltage curve is provided in Supplementary Fig. 26). We observe an electroluminescence EQE of up to 17.2%, which approaches the efficiency of the best-performing perovskite light-emitting diodes (LEDs), which are engineered specifically for efficient light emission^{48–50}. In addition, due to early sub-bandgap turn-on, probably from thermal carriers, our PSCs exhibit a peak electroluminescence ECE of up to 21.6%.

In addition to extremely low V_{OC} loss and high luminescence efficiency, our devices exhibit a high fill factor of up to 84.8%. Such a high fill factor is a result of improved carrier mobility in the perovskite active layer and better charge collection with the SnO₂ ETL developed here with minimum parasitic losses from shunt and series resistances. For a further improvement in fill factor, future research should be focused on minimizing trap-assisted recombination, aiming to approach the theoretical fill factor limit of about 90%.

Online content

Any methods, additional references, Nature Research reporting summaries, source data, extended data, supplementary information, acknowledgements, peer review information; details of author contributions and competing interests; and statements of data and code availability are available at <https://doi.org/10.1038/s41586-021-03285-w>.

- Burschka, J. et al. Sequential deposition as a route to high-performance perovskite-sensitized solar cells. *Nature* **499**, 316–319 (2013).
- Jeon, N. J. et al. Solvent engineering for high-performance inorganic-organic hybrid perovskite solar cells. *Nat. Mater.* **13**, 897–903 (2014).
- Yang, W. S. et al. Iodide management in formamidinium-lead-halide-based perovskite layers for efficient solar cells. *Science* **356**, 1376–1379 (2017).
- Jeon, N. J. et al. Compositional engineering of perovskite materials for high-performance solar cells. *Nature* **517**, 476–480 (2015).
- Abdi-Jalebi, M. et al. Maximizing and stabilizing luminescence from halide perovskites with potassium passivation. *Nature* **555**, 497–501 (2018).
- Saliba, M. et al. Incorporation of rubidium cations into perovskite solar cells improves photovoltaic performance. *Science* **354**, 206–209 (2016).
- Wang, Y. et al. Stabilizing heterostructures of soft perovskite semiconductors. *Science* **365**, 687–691 (2019).
- Yoo, J. J. et al. An interface stabilized perovskite solar cell with high stabilized efficiency and low voltage loss. *Energy Environ. Sci.* **12**, 2192–2199 (2019).
- Min, H. et al. Efficient, stable solar cells by using inherent bandgap of α -phase formamidinium lead iodide. *Science* **366**, 749–753 (2019).
- Jung, E. H. et al. Efficient, stable and scalable perovskite solar cells using poly(3-hexylthiophene). *Nature* **567**, 511–515 (2019).
- Krückemeier, L., Rau, U., Stolterfoht, M. & Kirchartz, T. How to report record open-circuit voltages in lead-halide perovskite solar cells. *Adv. Energy Mater.* **10**, 1902573 (2020).
- Shockley, W. & Queisser, H. J. Detailed balance limit of efficiency of p – n junction solar cells. *J. Appl. Phys.* **32**, 510–519 (1961).
- Jung, K. H., Seo, J. Y., Lee, S., Shin, H. & Park, N. G. Solution-processed SnO₂ thin film for a hysteresis-free planar perovskite solar cell with a power conversion efficiency of 19.2%. *J. Mater. Chem. A* **5**, 24790–24803 (2017).
- Shi, S. et al. Room-temperature synthesized SnO₂ electron transport layers for efficient perovskite solar cells. *RSC Adv.* **9**, 9946–9950 (2019).
- Li, J. et al. Enhanced crystallinity of low-temperature solution-processed SnO₂ for highly reproducible planar perovskite solar cells. *ChemSusChem* **11**, 2898–2903 (2018).

16. Jeong, S., Seo, S., Park, H. & Shin, H. Atomic layer deposition of a SnO_2 electron-transporting layer for planar perovskite solar cells with a power conversion efficiency of 18.3. *Chem. Commun.* **55**, 2433–2436 (2019).
17. Kam, M., Zhang, Q., Zhang, D. & Fan, Z. Room-temperature sputtered SnO_2 as robust electron transport layer for air-stable and efficient perovskite solar cells on rigid and flexible substrates. *Sci. Rep.* **9**, 6963 (2019).
18. Yun, A. J., Kim, J., Hwang, T. & Park, B. Origins of efficient perovskite solar cells with low-temperature processed SnO_2 electron transport layer. *ACS Appl. Energy Mater.* **2**, 3554–3560 (2019).
19. Jiang, Q. et al. Surface passivation of perovskite film for efficient solar cells. *Nat. Photon.* **13**, 460–466 (2019).
20. Rau, U. Reciprocity relation between photovoltaic quantum efficiency and electroluminescent emission of solar cells. *Phys. Rev. B* **76**, 085303 (2007).
21. Stolerohoff, M. et al. Voltage-dependent photoluminescence and how it correlates with the fill factor and open-circuit voltage in perovskite solar cells. *ACS Energy Lett.* **4**, 2887–2892 (2019).
22. Halvani Anaraki, E. et al. Low-temperature Nb-doped SnO_2 electron-selective contact yields over 20% efficiency in planar perovskite solar cells. *ACS Energy Lett.* **3**, 773–778 (2018).
23. Correa Baena, J. P. et al. Highly efficient planar perovskite solar cells through band alignment engineering. *Energy Environ. Sci.* **8**, 2928–2934 (2015).
24. Uchiyama, H., Ohgi, H. & Imai, H. Selective preparation of SnO_2 and SnO crystals with controlled morphologies in an aqueous solution system. *Cryst. Growth Design* **6**, 2186–2190 (2006).
25. Ibarguen, C. A., Mosquera, A., Parra, R., Castro, M. S. & Rodríguez-Páez, J. E. Synthesis of SnO_2 nanoparticles through the controlled precipitation route. *Mater. Chem. Phys.* **101**, 433–440 (2007).
26. Ghosh, S. & Roy, S. Effect of ageing on $\text{Sn}_6\text{O}_4(\text{OH})_4$ in aqueous medium—simultaneous production of SnO and SnO_2 nanoparticles at room temperature. *J. Sol-Gel Sci. Technol.* **81**, 769–773 (2017).
27. Wang, J. et al. Controlled synthesis of Sn-based oxides: via a hydrothermal method and their visible light photocatalytic performances. *RSC Adv.* **7**, 27024–27032 (2017).
28. Wang, H. et al. Engineering of facets, band structure, and gas-sensing properties of hierarchical Sn^{2+} -doped SnO_2 nanostructures. *Adv. Funct. Mater.* **23**, 4847–4853 (2013).
29. Han, D., Jiang, B., Feng, J., Yin, Y. & Wang, W. Photocatalytic self-doped SnO_{2-x} nanocrystals drive visible-light-responsive color switching. *Angew. Chem. Int. Ed.* **56**, 7792–7796 (2017).
30. Fan, C. M. et al. Synproportionation reaction for the fabrication of Sn^{2+} self-doped SnO_{2-x} nanocrystals with tunable band structure and highly efficient visible light photocatalytic activity. *J. Phys. Chem. C* **117**, 24157–24166 (2013).
31. Cohen, R. L. & West, K. W. Solution chemistry and colloid formation in the chloride sensitizing process. *J. Electrochem. Soc.* **119**, 433–438 (1972).
32. Matsuno, H., Kawashima, Y. & Serizawa, T. Peptide-induced formation of crystalline $\text{Sn}_6\text{O}_4(\text{OH})_4$ nanoparticles under ambient conditions. *Bull. Chem. Soc. Jpn.* **85**, 746–752 (2012).
33. Ning, J. et al. Facile synthesis of tin oxide nanoflowers: a potential high-capacity lithium-ion-storage material. *Langmuir* **25**, 1818–1821 (2009).
34. Li, N. et al. Effects of oxygen vacancies on the electrochemical performance of tin oxide. *J. Mater. Chem. A* **1**, 1536–1539 (2013).
35. Yang, Y., Wang, Y. & Yin, S. Oxygen vacancies confined in SnO_2 nanoparticles for desirable electronic structure and enhanced visible light photocatalytic activity. *Appl. Surf. Sci.* **420**, 399–406 (2017).
36. Sun, M., Su, Y., Du, C., Zhao, Q. & Liu, Z. Self-doping for visible light photocatalytic purposes: construction of $\text{SiO}_2/\text{SnO}_2/\text{SnO}_2:\text{Sn}^{2+}$ nanostructures with tunable optical and photocatalytic performance. *RSC Adv.* **4**, 30820–30827 (2014).
37. Wang, J. et al. Performance enhancement of perovskite solar cells with Mg-doped TiO_2 compact film as the hole-blocking layer. *Appl. Phys. Lett.* **106**, 121104 (2015).
38. Zhou, Y. et al. Manipulating crystallization of organolead mixed-halide thin films in antisolvent baths for wide-bandgap perovskite solar cells. *ACS Appl. Mater. Interf.* **8**, 2232–2237 (2016).
39. Kim, S., Eom, T., Ha, Y.-S., Hong, K.-H. & Kim, H. Thermodynamics of multicomponent perovskites: a guide to highly efficient and stable solar cell materials. *Chem. Mater.* **32**, 4265–4272 (2020).
40. Jeon, J. et al. Polymorphic phase control mechanism of organic-inorganic hybrid perovskite engineered by dual-site alloying. *J. Phys. Chem. C* **121**, 9508–9515 (2017).
41. Liu, Y. et al. Ultrahydrophobic 3D/2D fluorocarbon bilayer-based water-resistant perovskite solar cells with efficiencies exceeding 22%. *Sci. Adv.* **5**, eaaw2543 (2019).
42. Correa-Baena, J.-P. et al. Homogenized halides and alkali cation segregation in alloyed organic-inorganic perovskites. *Science* **363**, 627–631 (2019).
43. Rehman, W. et al. Charge-carrier dynamics and mobilities in formamidinium lead mixed-halide perovskites. *Adv. Mater.* **27**, 7938–7944 (2015).
44. Kim, D. H. et al. 300% enhancement of carrier mobility in uniaxial-oriented perovskite films formed by topotactic-oriented attachment. *Adv. Mater.* **29**, 1606831 (2017).
45. National Renewable Energy Laboratory Best Research-Cell Efficiencies <https://www.nrel.gov/pv/assets/pdfs/best-research-cell-efficiencies.20191106.pdf> (NREL, 2019).
46. Guillermo, J. F., Kirchartz, T., Cahen, D. & Rau, U. Guide for the perplexed to the Shockley–Queisser model for solar cells. *Nat. Photon.* **13**, 501–505 (2019).
47. Kiermasch, D., Gil-Escriv, L., Bolink, H. J. & Tvingstedt, K. Effects of masking on open-circuit voltage and fill factor in solar cells. *Joule* **3**, 16–26 (2019).
48. Lin, K. et al. Perovskite light-emitting diodes with external quantum efficiency exceeding 20 per cent. *Nature* **562**, 245–248 (2018).
49. Cao, Y. et al. Perovskite light-emitting diodes based on spontaneously formed submicrometre-scale structures. *Nature* **562**, 249–253 (2018).
50. Chiba, T. et al. Anion-exchange red perovskite quantum dots with ammonium iodine salts for highly efficient light-emitting devices. *Nat. Photon.* **12**, 681–687 (2018).

Publisher's note Springer Nature remains neutral with regard to jurisdictional claims in published maps and institutional affiliations.

© The Author(s), under exclusive licence to Springer Nature Limited 2021

Article

Reporting summary

Further information on research design is available in the Nature Research Reporting Summary linked to this paper.

Data availability

The data that support the findings of this study are available from the corresponding authors upon reasonable request.

Code availability

The LabView codes used in this work are available from the corresponding authors upon reasonable request.

Acknowledgements J.J.Y. was funded by the Institute for Soldier Nanotechnology (ISN) grant W911NF-13-D-0001 and the National Aeronautics and Space Administration (NASA) grant NNX16AM70H. Y.L. and M.G.B. were funded by Eni SpA through the MIT Energy Initiative. M.R.C. was funded by the Agency for Science Technology and Research, Singapore. V.B. was funded by Tata Trusts. T.G.P. and F.R. were funded by the National Research Foundation of Korea (NRF-2019R1A2C3003504) and a National Research Council of Science & Technology (NST) grant from the Korean government (MSIT) (grant number CAP-18-05-KAERI). G.S., S.S.S., C.S.M., N.J.J. and J.S. were supported by a grant from the Korea Research Institute of Chemical Technology (KRICT), South Korea (KS2022-10); the Korea Institute of Energy Technology Evaluation and

Planning (KETEP) and the Ministry of Trade Industry & Energy (MOTIE) of South Korea (grant number 20183010014470); by a grant from the National Research Foundation of Korea (NRF) funded by the Ministry of Science, ICT & Future Planning (MSIP) of South Korea (NRF-2016M3A6A7945503) and by a grant from the NST from the Korean government (MSIT) (grant number CAP-18-05-KAERI). We thank S.-M. Bang, G. Kim, K. Kim, J. Kim and J. Park for discussions and assistance with the experiments. We thank KARA (KAIST Analysis center for Research Advancement) for their assistance with X-ray photoelectron spectroscopy and ultraviolet photoelectron spectroscopy measurements and analysis.

Author contributions J.J.Y., G.S. and S.S.S. conceived and designed the experiment. G.S. and S.S.S. conducted the synthesis and the analysis of the SnO₂ film along with J.-P.C.-B. J.J.Y. and Y.L. performed the characterization of the perovskite films. J.J.Y., G.S. and S.S.S. conducted the fabrication of perovskite solar cells and their certification. Y.-K.K. conducted the TEM analysis. M.R.C. conducted the electroluminescence measurements with supervision from V.B. C.S.M. conducted the transient photovoltage and transient photocurrent measurements. T.G.P. performed the optical pump–terahertz probe measurements with supervision from F.R. J.J.Y. and G.S. wrote the first draft of the manuscript and all authors contributed feedback and comments. N.J.J. synthesized materials for perovskite film. S.S.S., M.G.B. and J.S. directed and supervised the research.

Competing interests The authors declare no competing interests.

Additional information

Supplementary information The online version contains supplementary material available at <https://doi.org/10.1038/s41586-021-03285-w>.

Correspondence and requests for materials should be addressed to S.S.S., M.G.B. or J.S.

Peer review information *Nature* thanks the anonymous reviewer(s) for their contribution to the peer review of this work.

Reprints and permissions information is available at <http://www.nature.com/reprints>.

Solar Cells Reporting Summary

Nature Research wishes to improve the reproducibility of the work that we publish. This form is intended for publication with all accepted papers reporting the characterization of photovoltaic devices and provides structure for consistency and transparency in reporting. Some list items might not apply to an individual manuscript, but all fields must be completed for clarity.

For further information on Nature Research policies, including our [data availability policy](#), see [Authors & Referees](#).

► Experimental design

Please check: are the following details reported in the manuscript?

1. Dimensions

Area of the tested solar cells

<input checked="" type="checkbox"/> Yes	Main text, method section, and Figure 4 caption
<input type="checkbox"/> No	
<input checked="" type="checkbox"/> Yes	Figure 4 caption
<input type="checkbox"/> No	

2. Current-voltage characterization

Current density-voltage (J-V) plots in both forward and backward direction

<input checked="" type="checkbox"/> Yes	Main text and method section
<input type="checkbox"/> No	

Voltage scan conditions

For instance: scan direction, speed, dwell times

<input checked="" type="checkbox"/> Yes	Main text and method section
<input type="checkbox"/> No	

Test environment

For instance: characterization temperature, in air or in glove box

<input type="checkbox"/> Yes	Main text and method section
<input checked="" type="checkbox"/> No	

Protocol for preconditioning of the device before its characterization

<input type="checkbox"/> Yes	No preconditioning protocol was involved during testing
<input checked="" type="checkbox"/> No	

Stability of the J-V characteristic

Verified with time evolution of the maximum power point or with the photocurrent at maximum power point; see ref. 7 for details.

<input checked="" type="checkbox"/> Yes	Figure 2
<input type="checkbox"/> No	

3. Hysteresis or any other unusual behaviour

Description of the unusual behaviour observed during the characterization

<input type="checkbox"/> Yes	No unusual hysteric behavior is observed
<input checked="" type="checkbox"/> No	

Related experimental data

<input type="checkbox"/> Yes	No unusual hysteric behavior is observed
<input checked="" type="checkbox"/> No	

4. Efficiency

External quantum efficiency (EQE) or incident photons to current efficiency (IPCE)

<input checked="" type="checkbox"/> Yes	Supplementary Figure 24
<input type="checkbox"/> No	

A comparison between the integrated response under the standard reference spectrum and the response measure under the simulator

<input checked="" type="checkbox"/> Yes	Supplementary Figure 24
<input type="checkbox"/> No	

For tandem solar cells, the bias illumination and bias voltage used for each subcell

<input type="checkbox"/> Yes	No tandem work is reported
<input checked="" type="checkbox"/> No	

5. Calibration

Light source and reference cell or sensor used for the characterization

<input checked="" type="checkbox"/> Yes	Method section and on the certification document
<input type="checkbox"/> No	

Confirmation that the reference cell was calibrated and certified

<input checked="" type="checkbox"/> Yes	Method section and on the certification document
<input type="checkbox"/> No	

Calculation of spectral mismatch between the reference cell and the devices under test

- Yes On the certificate
 No

6. Mask/aperture

Size of the mask/aperture used during testing

- Yes Main text, method section, and on the certificate
 No

Variation of the measured short-circuit current density with the mask/aperture area

- Yes The mask size was not varied
 No

7. Performance certification

Identity of the independent certification laboratory that confirmed the photovoltaic performance

- Yes Supplementary Figure 9 and 20
 No

A copy of any certificate(s)

Provide in Supplementary Information

- Yes Supplementary Figure 9 and 20
 No

8. Statistics

Number of solar cells tested

- Yes Supplementary Figure 5, 6, 7, and 19
 No

Statistical analysis of the device performance

- Yes Supplementary Figure 5, 6, 7, and 19
 No

9. Long-term stability analysis

Type of analysis, bias conditions and environmental conditions

For instance: illumination type, temperature, atmosphere humidity, encapsulation method, preconditioning temperature

- Yes Methods section and Supplementary Figure 23
 No